RSC Advances

Check for updates

Facile synthesis of perovskite CeMnO₃ nanofibers as an anode material for high performance lithium-ion batteries

Bin Yue,† Quanli Hu, [ID] †* Lei Ji, Yin Wang and Jinghai Liu [ID] *

A facile synthesis of perovskite-type CeMnO₃ nanofibers as a high performance anode material for lithium-ion batteries was demonstrated. The nanofibers were prepared by the electrospinning technique. The characterization of CeMnO₃ nanofibers was carried out by X-ray diffraction, Fourier transform infrared spectroscopy, scanning electron microscopy (SEM), transmission electron microscopy (TEM), and X-ray photoelectron spectroscopy. SEM images manifested nanofibers with a diameter of 470 nm having a rough surface with a porous structure. TEM images were consistent with the observations from the SEM images. The electrochemical properties of CeMnO₃ perovskite in lithium-ion batteries were investigated. The CeMnO₃ anode exhibited a discharge capacity of 2159 mA h g^{-1} with a coulombic efficiency of 93.79%. In addition, a high cycle stability and a capacity of 276 mA h g^{-1} at the current density of 1000 mA g^{-1} can be effectively maintained due to the high Li$^+$ conductivity in the CeMnO₃ anode. This study could provide an efficient and potential application of perovskite-type CeMnO₃ nanofibers in lithium-ion batteries.

Introduction

With the rapid development of science and technology, electronic equipment has also undergone exponential evolution during the past 5 decades. The electrical power unit (EPU) makes people's life more convenient. In the meantime, it leads to many serious issues, such as the damage and pollution of the environment. It is extremely urgent to develop environmentally friendly and efficient energy storage systems for current electric vehicles.[1] The lithium-ion battery (LIB) is one of the most desired electrochemical energy storage devices thanks to its high voltage, high energy density, small self-discharge, long cycle retention, no-memory effect, and eco-friendliness. At present, graphite is the most common anode material for the commercial LIBs with a relatively low theoretical specific capacity of 372 mA h g^{-1}.[2] The slow evolution of electrode materials seriously restricts the further development of LIBs commercialization. Therefore, in the cause of meeting market requirements, it is an emergency to develop anode materials having high energy density, high safety, and long cycle life for high performance energy storage system.[3–9]

So far, many researchers have studied a variety of materials for high performance LIB anodes. Silicon has attracted much attention thanks to the ultra-high theoretical specific capacity (4200 mA h g^{-1}). However, there is a critical issue that the large volume expansion ratio limits its application in LIBs.[10–12] It was reported that transition metal oxides exhibited favorable electrochemical performances as anode materials for LIBs, such as Co$_x$O$_y$,[13–16] Fe₃O₄,[17,18] Ni$_x$O$_y$,[19,20] and Mn$_x$O$_y$.[21,22] Specially, Mn$_x$O$_y$ is regarded as a promising material for LIB anode owing to abundance, low cost, and eco-friendliness.[23] But low conductivity gives rise to structural collapse of the anode material during Li$^+$ ion insertion/deinsertion, leading to poor cycle stability.[24–27] For purpose of solving this critical issue, researchers focused on improving the conductivity of anode material. Graphene-wrapped MnO₂ nanoribbons synthesized by hydrothermal reaction showed a specific capacity of 890 mA h g^{-1} at a current density of 100 mA g^{-1}.[28] The chemically fabricated coaxial MnO₂/CNT nanocomposites presented a specific capacity of 474 mA h g^{-1} at a current density of 1600 mA g^{-1}.[29] In addition, MnO₂@TiO₂ nanocomposites with core@shell structure, which greatly improved the anode stability, presented a specific capacity of 938 mA h g^{-1} at a current density of 300 mA g^{-1}.[30] As a stable oxide, CeO₂ is used in the fields of electronic devices, catalysis, and electrochemical energy storage due to its favorably thermal stability, catalytic activity, and suitable valence states.[31–33] The charge mass transfer resistance is greatly reduced, and the electrochemical performance is highly improved by constructing ternary perovskite structure.[34] Till now, the application of CeMnO₃ nanofibers with perovskite structure in lithium-ion batteries has not been studied.

Nano Innovation Institute (NII), Inner Mongolia Key Lab of Carbon Nanomaterials, College of Chemistry and Chemical Engineering, Inner Mongolia University for Nationalities (IMUN), Tongliao, 028-000, People's Republic of China. E-mail: huquanly@hotmail.com; jhliu2008@sinano.ac.cn

† These authors contributed equally to this work.

In this work, a facile synthesis of perovskite-type $CeMnO_3$ nanofibers by electrospinning technique as high performance anode material for lithium-ion batteries was demonstrated. This technique is easy to operate and applicable to synthesize many kinds of nanomaterials. Those nanofibers showed rough surface with mesoporous structure. The surface area and pore volume of $CeMnO_3$ are 108.772 m^2 g^{-1} and 0.176 cm^3 g^{-1}, respectively. The high surface area and mesoporous structure facilitate the penetration of electrolyte and the diffusion of Li$^+$ to the active electrode material. $CeMnO_3$ anode exhibited a discharge capacity of 2159 mA h g^{-1} with the coulombic efficiency of 93.79%. And a high reversible capacity of 395 mA h g^{-1} at 200 mA g^{-1} for $CeMnO_3$ can be obtained even at a high discharge rate of 1000 mA g^{-1} after 60 cycles. The perovskite $CeMnO_3$ with nanofiber-like structure exhibits favorable electrochemical behaviors. The layered structure from Mn–O octahedra in perovskite facilitates the insertion and extraction of Li$^+$. In addition, $CeMnO_3$ with perovskite structure improves the diffusion of Li$^+$, alleviates the structure collapse resulting from Li$^+$ insertion and extraction, and enhances the cycle stability. It indicates the potential application of perovskite-type $CeMnO_3$ nanofibers for lithium-ion batteries.

Experimental

The $CeMnO_3$ nanofibers were fabricated by effective electrospinning technique at room temperature and subsequent calcination process at 500 °C. Cerium nitrate hexahydrate ($Ce(NO_3)_3 \cdot 6H_2O$, 1.086 g) and manganese acetate (MnAc, 0.4326 g) were served as the sources of Ce and Mn. Polyvinylpyrrolidone (PVP, $M_w \approx 1\,300\,000$, 2.25 g) was worked as nanofiber template. N,N-dimethylformamide (DMF, 16.5 mL) was used as the solvent. The precursor solution was prepared by mixing $Ce(NO_3)_3 \cdot 6H_2O$, MnAc, and PVP into DMF, and stirring for 14 h. Then, this brownish solution was loaded into a 10 mL plastic syringe and electrospun at 18 kV with the distance between a collector and a needle of 15 cm at the flow rate of 0.75 mL h^{-1}. The as-spun $Ce(NO_3)_3$–MnAc/PVP nanofibers were dried at 55 °C overnight in a vacuum oven. The calcination process was performed at 500 °C for 2 h with a heating rate of 1 °C min^{-1} in a muffle furnace under air atmosphere. In addition, control samples of CeO_2 and Mn_3O_4 nanofibers was fabricated under the same condition without Mn and Ce source, respectively.

Brunauer–Emmett–Teller and Barrett–Joyner–Halenda (BET and BJH, Quadrasorbsi) methods were performed to determine the specific surface area and pore size distribution of $CeMnO_3$ NFs. The crystal structures of $CeMnO_3$, CeO_2, and Mn_3O_4 were studied using X-ray diffractometer (XRD, Bruker D8 Focus) at room temperature. The Fourier transforms infrared (FT-IR, Bruker Vector 22 Spectrometer) spectra of as-spun $Ce(NO_3)_3$–MnAc/PVP NFs and $CeMnO_3$ NFs were detected in the range from 4000 to 400 cm^{-1} using KBr as dispersant. The microstructures and morphologies of $CeMnO_3$ NFs were analyzed on a scanning electron microscope (SEM, Hitachi S-4800, 20 kV) and a transmission electron microscope (TEM, JEOL JEM 2100, 200 kV). X-ray photoelectron spectroscopy (XPS, Al Kα, Thermo

Escalab 250) was carried out to analyze the valence states of $CeMnO_3$ NFs.

The electrochemical characteristics of CeO_2, Mn_3O_4, and $CeMnO_3$ were performed by assembling 2032-type coin cells. Electrodes were fabricated by adding $CeMnO_3$ (80 wt%), acetylene black (10 wt%), and polytetrafluoroethylene (PTFE, 10 wt%) into N-methyl-2-pyrrolidone (NMP) to form a homogeneous slurry. Then, the slurry was roll-pressed on aluminum foil and dried at 60 °C overnight in a vacuum oven. Electrochemical cells were fabricated with an active material as an anode, a lithium foil as a cathode, a Celgard 2400 microporous membrane as a separator, and 1 mol L^{-1} LiPF$_6$ as electrolyte solution. Those cells were assembled in an Ar-filled glove box with both oxygen and moisture content below 1 ppm (Vigor, Co. Ltd., Suzhou, China). Galvanostatic charge/discharge behaviors of CeO_2, Mn_3O_4, and $CeMnO_3$ were detected using a battery testing system (Land Co. Ltd., Wuhan, China) with a voltage window of 0.01–3.0 V vs. Li/Li$^+$ for setting current rates. Electrochemical impedance spectroscopy (EIS) measurements were implemented via an electrochemical workstation (Bio-Logic, Co. Ltd, Seyssinet-pariset, France). The AC perturbation signal was 5 mV with the frequency ranging from 0.01 to 10^5 Hz. Impedance data were analyzed using an electrochemical impedance software of EC-Lab.

Results and discussion

According to BET and BJH methods, the surface area and pore volume of $CeMnO_3$ are 108.772 m^2 g^{-1} and 0.176 cm^3 g^{-1}, respectively. In addition, the average pore diameter is 4.89 nm, indicating the mesoporous structure. The high surface area is of great importance to facilitate the diffusion of Li$^+$ from electrolyte to electrode material. The schematic illustration of $CeMnO_3$ with perovskite structure is depicted as shown in Fig. 1. The crystal structures of $CeMnO_3$, CeO_2, and Mn_3O_4 were recorded by XRD pattern which are displayed in Fig. 2(a). For CeO_2 sample, the diffraction peaks are assigned to (111), (200), (220), (311), (222), (400), (331) and (420) planes of cubic fluorite CeO_2. The XRD pattern matches well with the JCPDS card (34-0394) implying a face-centered cubic fluorite structure of CeO_2 with space group $Fm\bar{3}m$.[35] The diffraction peaks of Mn_3O_4 are related to (112), (200), (103), (211), (004), (220), (105), (303), (321), (224), and (400), which are agree with the JCPDS card (24-0734).[36] For $CeMnO_3$ NFs, the diffraction peaks slightly transfer to higher Bragger angle and the intensities become weaker and broader. The four major diffraction peaks of $CeMnO_3$ correspond to the (111) plane of CeO_2 and the (022), (02-2), and (220) planes of $CeMnO_3$.[37–39] The FT-IR spectra of as-spun $Ce(NO_3)_3$–MnAc/PVP NFs and $CeMnO_3$ NFs are depicted in Fig. 2(b). The peaks at 3434 and 1625 cm^{-1} correspond to the stretching and vibration mode of O–H. The peak at 2919 cm^{-1} is assigned to the stretching C–H vibration of alkyl groups. The peaks at 1651, 1438, and 1259 cm^{-1} are ascribed to C=O, C–H, and C–N functional groups.[40–42] Those peaks from $Ce(NO_3)_3$–MnAc/PVP NFs after calcination were weakened or vanished. The peaks at 520 and 433 cm^{-1} refer to the metal–oxygen stretching vibrations of Ce–O and Mn–O.[40,43]
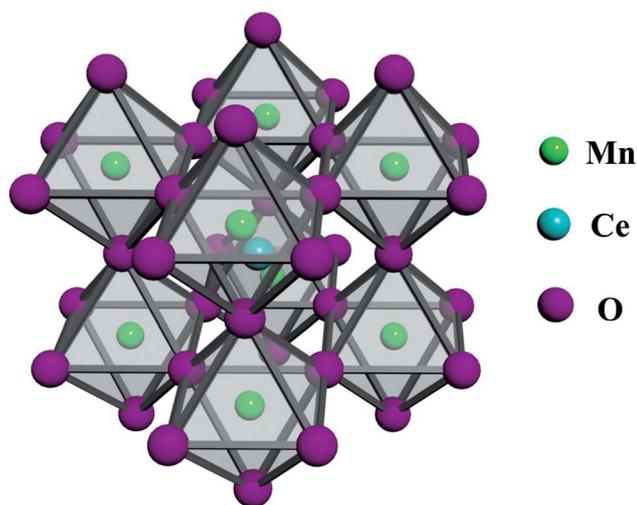
Fig. 1 The schematic structure of perovskite-type $CeMnO_3$.

The SEM images of $Ce(NO_3)_3$–MnAc/PVP NFs and $CeMnO_3$ NFs are shown in Fig. 3. The morphology of the precursor NFs was beige and uniform with the diameter of 550 nm. After calcination, the surfaces of $CeMnO_3$ NFs were no longer smooth, and those nanofibers were broken up into sections which could be originated from the combustion of PVP, the decomposition of nitrate and acetate, and the crystallization of Ce–Mn–O.[35,44] The diameter was reduced to 470 nm. The nanofiber-like structure provides a short diffusion path for ion transport.[45] The detailed morphology and structure of an individual $CeMnO_3$ NF were further investigated by TEM micrographs (Fig. 4). The TEM images indicate that the diameter of the individual nanofiber is 470 nm. The nanofiber shows rough surface with porous structure, which is greatly agree with the observations from SEM images.

The chemical bonding states and compositions of the fabricated $CeMnO_3$ NFs have been detected as shown in Fig. 5. In the survey spectrum, the peaks of O 1s, Mn 2P, Ce 3d, and Ce 4d have been shown in Fig. 5(a). Ce 3d spectrum was analyzed as shown in Fig. 5(b). Six major peaks can be observed, including three peaks at 882.32, 888.73, and 898.1 eV corresponding to the component of Ce $3d_{5/2}$, and three peaks at 900.71, 907.33, and

916.49 eV being assigned to the component of Ce $3d_{5/2}$.[46] It confirms the existence of Ce^{4+} in the $CeMnO_3$ NFs.[47] The detailed information of Ce 3d spectra is shown in Table 1. The binding energy peak at 108.6 eV with the component of Ce $4d_{5/2}$ from final state of $4d^9 4f^1 + 4d^9 4f^2$ can be clearly seen in Ce 4d spectrum (Fig. 5(c)), indicating the presence of Ce^{3+}.[49] Mn 2p spectrum is exhibited in Fig. 5(d). Two major peaks at 642.18 and 653.99 eV are assigned to the component of Mn $2p_{3/2}$ and Mn $2p_{1/2}$, respectively, implying the existence of Mn^{3+}.[50] As shown in Fig. 5(e), the main O 1s peaks at 529.73 and 530.90 eV are related to the oxygen atoms in the lattice and the oxygen ions of the oxygen deficient region in $CeMnO_3$ NFs, respectively.[51]

To further clarify the electrochemical performances of CeO_2, Mn_3O_4, and $CeMnO_3$ anodes, CV curves of electrodes for the 1st, 2nd and 5th cycles were analyzed. In Fig. 6(a), two reduction peaks V1 and V2 located at 0.2 and 0.6 V are detected in the first scan, which originated from the formation of solid electrolyte interphase (SEI) and the initial reduction of CeO_2 to Ce ($CeO_2 + 4Li^+ + 4e^- = Ce + 2Li_2O$), respectively. The oxidation peak at about 2.5 V (V3) as a result of the reaction between Ce and Li_2O ($Ce + 2Li_2O = CeO_2 + 4Li^+ + 4e^-$).[52] In Fig. 6(b), the major cathodic peaks in the 1st cycle for Mn_3O_4 located at 0.2 and 1.35 V. And the peak at 0.2 V is related to the formation of SEI layer and the reduction of Mn_xO_y with Li ions, which can be depicted by $Mn_3O_4 + 8Li^+ + 8e^- = 3Mn + 4Li_2O$.[53] After five repetitive cycles, the oxidation-reduction peaks decreased slightly, and a good stability can be carefully maintained. As show in Fig. 6(c), compared with CeO_2 and Mn_3O_4, $CeMnO_3$ shows relatively different peak positions. The oxidation peaks at 1.2 and 2.4 V are attributed to the oxidation of Ce^{3+} and Mn^{3+}, and there is a wide plateau at 0.5–1.0 V, which originates from the reduction of Mn^{3+} to metallic Mn.[54] A small CV curve was shown in the first cycle, which might be due to the super ion-conduction of perovskite $CeMnO_3$.

Fig. 7 displays the initial discharge profiles of CeO_2, Mn_3O_4, and $CeMnO_3$ anodes. The cells were charged and discharged at a current density of 200 mA g^{-1} in the voltage range of 0.01–3.0 V *versus* Li^+/Li. The three fabricated samples exhibit discharge capacities of 338, 592, 2159 mA h g^{-1} with coulombic efficiencies of 94.67%, 84.63%, and 93.79%, respectively. The
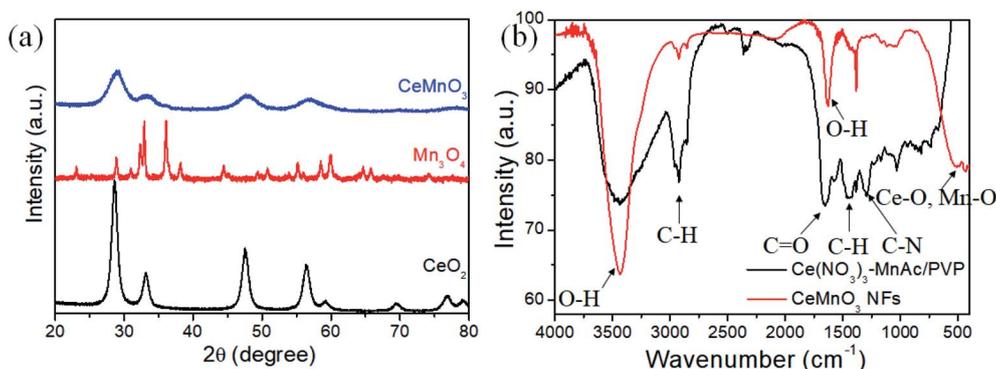

Fig. 2 (a) XRD patterns of CeO_2, Mn_3O_4, and $CeMnO_3$ NFs. (b) FT-IR spectra of as-spun $Ce(NO_3)_3$–MnAc/PVP NFs and $CeMnO_3$ NFs.
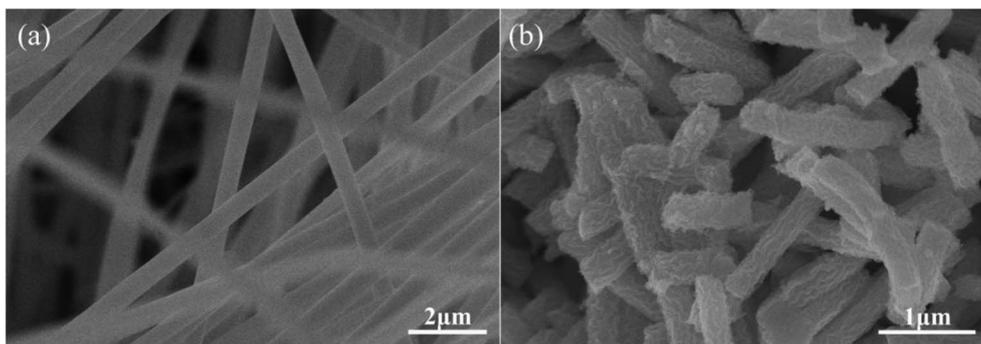
Fig. 3 (a) SEM image of as-spun Ce(NO$_3$)$_3$−MnAc/PVP NFs. (b) SEM image of CeMnO$_3$ NFs.

SEI layer formed between electrode and electrolyte leads to the irreversible capacity reduction in the first cycle.[55] From the discharge curve, CeO$_2$ and Mn$_3$O$_4$ cells exhibit considerably narrow discharge platforms. However, it is obvious that perovskite CeMnO$_3$ has a relatively stable discharge platform at 0.5 V. As shown in Fig. 1, the layered structure from Mn–O octahedra is constructed by sharing one oxygen atom. Between the layers, the insertion and deinsertion of Li$^+$ can achieve from this perovskite structure.[33] Therefore, CeMnO$_3$ NFs exhibit high reversible capacity compared with the other two samples.

The cycling performances of CeO$_2$, Mn$_3$O$_4$, and CeMnO$_3$ anodes under a current density of 200 mA g^{-1} with the voltage ranging from 0.01 to 3.0 V are presented in Fig. 8. Within 20 cycles, the capacities of the three samples rapidly declined. The discharge specific capacity of CeO$_2$ reduces to lower than 200 mA h g^{-1} after ten cycles and that of Mn$_3$O$_4$ after 20 cycles is about 300 mA h g^{-1}. Due to the Jahn–Teller effect, Mn^{3+} is gradually converted into Mn^{2+} and Mn^{4+}, and then dispersed in the electrolyte, resulting in irreversible capacity reduction after consecutive cycling. A stable capacity can be achieved in CeMnO$_3$ anode. For CeMnO$_3$ anode, after 60 cycles the capacity gradually increases, because the anode undergoes a rapid activation process.[56] The reaction of CeMnO$_3$ + Li$_2$O = CeO$_2$ + MnO$_2$ + 2Li$^+$ + 2e$^-$ is gradually strengthened, which further improves the electrochemical performance. Compared with Mn$_3$O$_4$, the unique perovskite structure of CeMnO$_3$ can improve the diffusion of Li$^+$, alleviate the structure collapse resulting from Li$^+$ insertion and extraction, and improve the cycle stability.[33] After

200 cycles the capacities of CeO$_2$, Mn$_3$O$_4$, and CeMnO$_3$ anode are 175.6, 315 and 322.9 mA h g^{-1}, respectively. In comparison with common CeO$_2$ with the reversible capacity of 315 mA h g^{-1} after 50 cycles, the fabricated CeMnO$_3$ as anode material exhibits more stable cycle life and higher capacity.[57]

Fig. 9 exhibits the rate capabilities of CeO$_2$, Mn$_3$O$_4$ and CeMnO$_3$. The three kinds of assembled cells were measured at the current density of 200 mA g^{-1} in the first 10 cycles, and then measured at various current densities ranging from 400 to 1000 mA g^{-1}. Among the three samples, CeMnO$_3$ displays the best performance and the highest reversible capacity of 530 mA h g^{-1} at the current density of 200 mA g^{-1} after 10 cycles. When the current densities increased, the capacity slightly decreased. Particularly, after discharging at 1000 mA g^{-1}, CeMnO$_3$ anode still presents a reversible discharge capacity of 276 mA h g^{-1}. Furthermore, an ultra-high reversible capacity of 395 mA h g^{-1} at 200 mA g^{-1} can be obtained even at a high discharge rate of 1000 mA g^{-1} after 60 cycles. As illustrated in Fig. 10, the sloping line in the low frequency region is ascribed to Warburg impedance (Z_w).[58] The R_{ct} value of CeMnO$_3$ is 36.78 Ω, which is much lower than those of CeO$_2$ (49.18 Ω) and Mn$_3$O$_4$ (67.99 Ω), implying the high conductivity of the electrochemical system consisting of CeMnO$_3$. In order to further clarify the Li$^+$ diffusion performance, the Warburg impedance (Z_w) for the equivalent circuit (as illustrated in the inset of Fig. 10), the exchange current density ($i°$) and the diffusion coefficient of Li$^+$ (D) can be depicted by the following equation.[59]
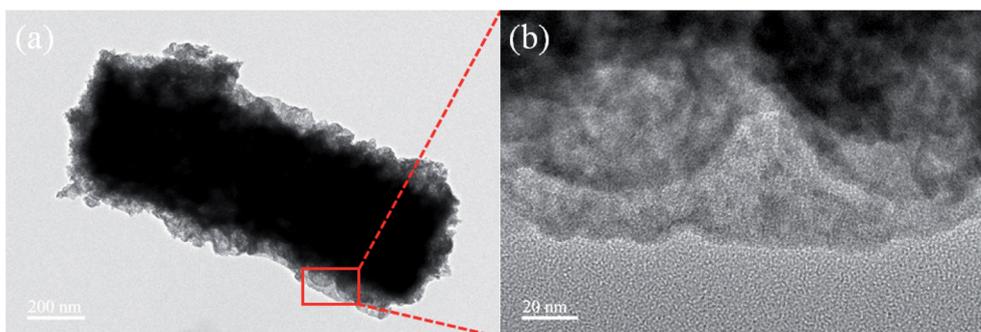

Fig. 4 (a) TEM image and (b) high resolution TEM image of CeMnO$_3$ NF.
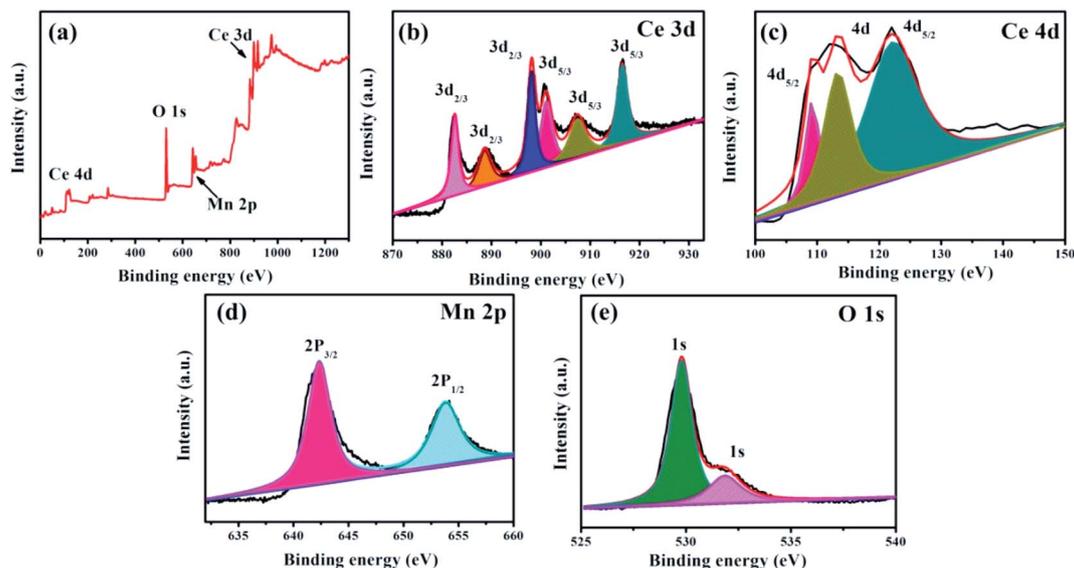
Fig. 5 XPS spectra CeMnO$_3$ NFs: (a) survey scan, (b) Ce 3d region, (c) Ce 4d region, (d) Mn 2p region, and (e) O 1s region.

Table 1 Information of the Ce 3d spectrum of XPS[46–48]

Ce contribution	Peak position (eV)	Peak characteristics	Final state
Ce(IV)	882.32	3d$_{5/2}$	3d^{9}4f^2
Ce(IV)	888.73	3d$_{5/2}$	3d^{9}4f^1
Ce(IV)	898.1	3d$_{5/2}$	3d^{9}4f^0
Ce(IV)	900.71	3d$_{3/2}$	3d^{9}4f^2
Ce(IV)	907.33	3d$_{3/2}$	3d^{9}4f^1
Ce(IV)	916.49	3d$_{3/2}$	3d^{9}4f^0

$$|Z| = R_e + R_{ct} + \sigma\omega^{-1/2} \quad (1)$$

$$D = \frac{R^2 T^2}{2A^2 n^4 F^4 C^2 \sigma^2} \quad (2)$$

$$i° = \frac{RT}{nFR_{ct}} \quad (3)$$

where, ω is the angular frequency, R is ideal gas constant, n is number of transfer charge, F is the Faraday constant, and C is the concentration of Li$^+$. σ is the Warburg coefficient which can be calculated from the slope of the Bode plot (as show in
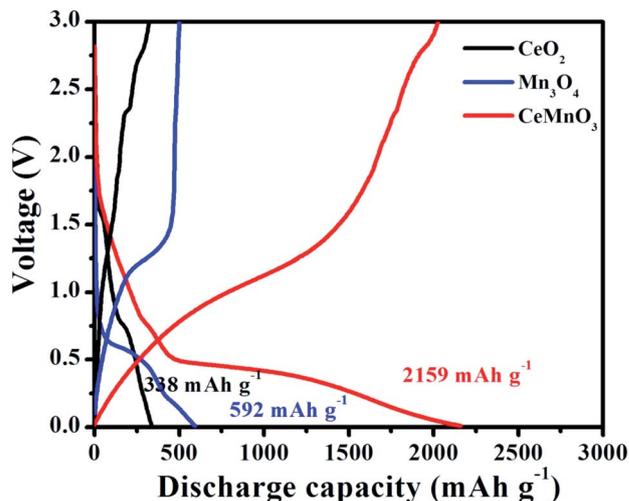

Fig. 7 The initial charge–discharge profiles of CeO$_2$, Mn$_3$O$_4$, and CeMnO$_3$ in the voltage of 0.01–3.0 V.

Fig. 11). CeMnO$_3$ exhibits the highest Li$^+$ diffusion coefficient of 6.7261×10^{-16} cm^2 s^{-1}. It confirms that CeMnO$_3$ anode exhibits a favorable Li$^+$ diffusion performance. The detailed
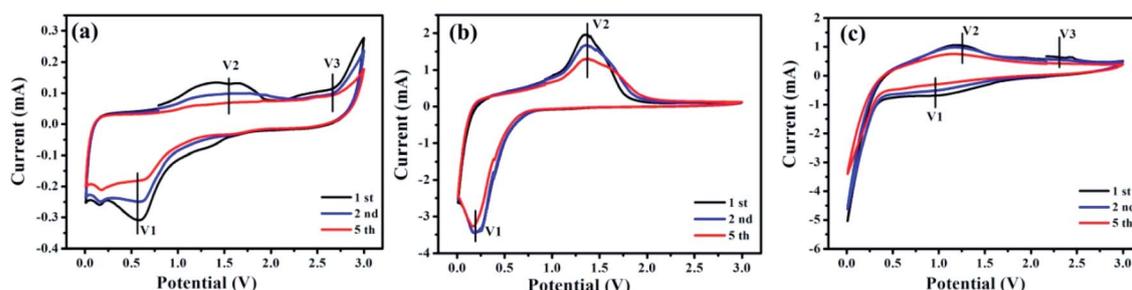

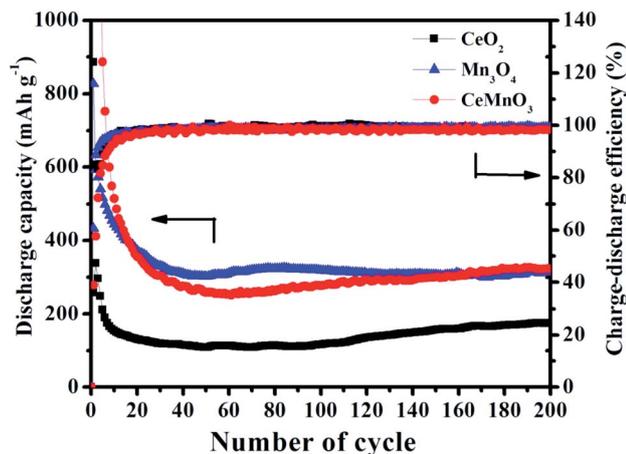**Fig. 6** CV curves of electrodes for 1st, 2nd and 5th cycles at a scan rate of 0.05 mV s^{-1} of (a) CeO$_2$, (b) Mn$_3$O$_4$, and (c) CeMnO$_3$.

Fig. 8 The cycle capabilities of CeO_2, Mn_3O_4, and $CeMnO_3$ at 200 mA g^{-1} in the voltage range of 0.01–3.0 V.
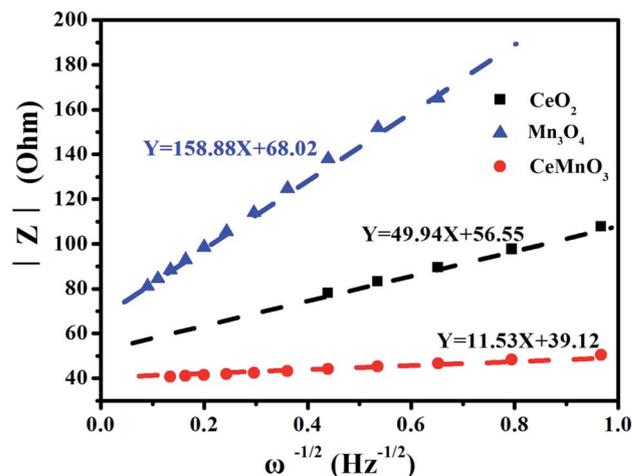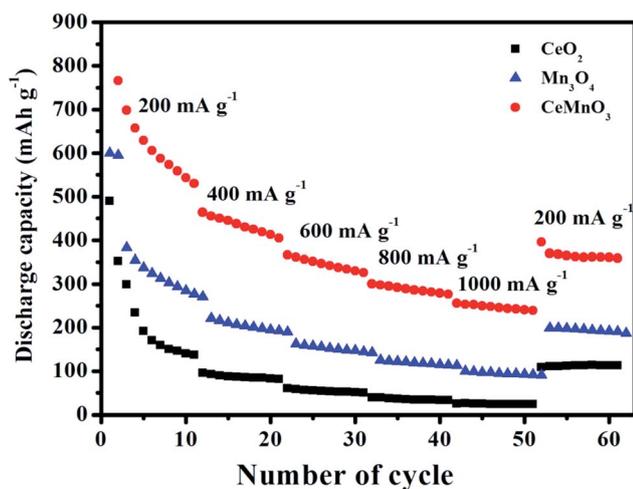

Fig. 9 Rate performance of as-prepared CeO_2, Mn_3O_4, and $CeMnO_3$.
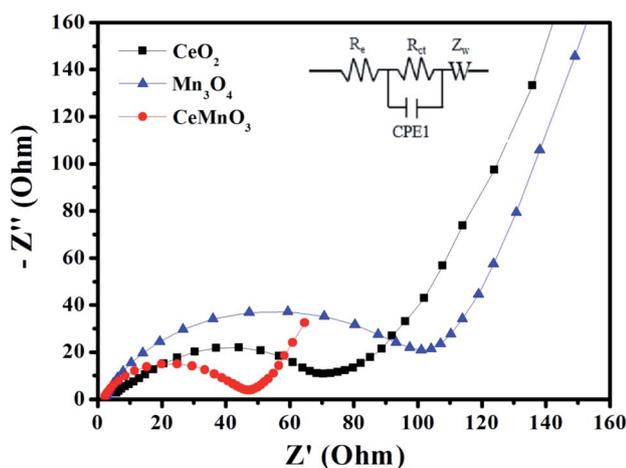

Fig. 10 Impedance spectra of CeO_2, Mn_3O_4, and $CeMnO_3$ at open circuit voltage. Inset: equivalent circuit corresponding to the impedance diagrams.

Fig. 11 Fitting line of the |Z| vs. $\omega^{-1/2}$ relationship of CeO_2, Mn_3O_4, and $CeMnO_3$.

Table 2 Electrochemical impedance parameters of CeO_2, Mn_3O_4, and $CeMnO_3$

Sample	R_e (Ω)	R_{ct} (Ω)	σ (Ω s$^{-0.5}$)	D (cm^2 s^{-1})	i° (mA cm^2)
CeO_2	7.669	49.18	49.94	3.5876×10^{-17}	5.2134×10^{-4}
Mn_3O_4	2.99	67.99	158.88	3.5423×10^{-18}	3.8293×10^{-4}
$CeMnO_3$	2.596	36.78	11.53	6.7261×10^{-16}	7.0787×10^{-3}

electrochemical impedance parameters of CeO_2, Mn_3O_4, and $CeMnO_3$ anodes were summarized in Table 2.

The perovskite $CeMnO_3$ with nanofiber-like structure present favorable electrochemical behaviors. The perovskite structure facilitates the insertion of Li$^+$ into Ce-site vacancies and stabilize the cycling performance after the initial discharge process.[60] The nanofiber-like structure can effectively improve the contact area between electrolyte and anode and shorten the path of Li$^+$ entering anode material, thus reducing the electrochemical impedance of the material.[61]

Conclusions

Perovskite-type $CeMnO_3$ nanofibers as high performance anode material for lithium-ion batteries was effectively synthesized by electrospinning process. These nanofibers with a diameter of 470 nm present rough surface with mesoporous structure. The electrochemical properties of $CeMnO_3$ perovskite in lithium-ion batteries were investigated. $CeMnO_3$ anode exhibited a discharge capacity of 2159 mA h g^{-1} with a coulombic efficiency of 93.79%. A high reversible capacity of 395 mA h g^{-1} at 200 mA g^{-1} for $CeMnO_3$ can be obtained even at a high discharge rate of 1000 mA g^{-1} after 60 cycles. This study provides the feasibility of perovskite-type $CeMnO_3$ nanofibers for the application into lithium-ion batteries. This result opens a new path for a more efficient and convenient chemical storage method in the near future.

Conflicts of interest

There are no conflicts to declare.

Acknowledgements

References

1 A. Fotouhi, D. J. Auger, K. Propp, S. Longo and M. Wild, A review on electric vehicle battery modelling: from lithium-ion toward lithium–sulphur, *Renewable Sustainable Energy Rev.*, 2016, **56**, 1008–1021.

2 J. Ma, F. Yu, Z. Wen, M. Yang, H. Zhou, C. Li, L. Jin, L. Zhou, L. Chen, Z. Yuan and J. Chen, A facile one-pot method for synthesis of low-cost iron oxide/activated carbon nanotube electrode materials for lithium-ion batteries, *Dalton Trans.*, 2013, **42**, 1356–1359.

3 Y. Zhao, X. Li, B. Yan, D. J. Li, S. Lawes and X. L. Sun, Significant impact of 2D graphene nanosheets on large volume change tin-based anodes in lithium-ion batteries: a review, *J. Power Sources*, 2015, **274**, 869–884.

4 Y. Deng, C. Fang and G. Chen, The developments of SnO_2/graphene nanocomposites as anode materials for high performance lithium ion batteries: a review, *J. Power Sources*, 2016, **304**, 81–101.

5 N. Nitta, F. Wu, J. T. Lee and G. Yushin, Li-ion battery materials: present and future, *Mater. Today*, 2015, **18**, 252–264.

6 W. Shi, J. Mao, X. Xu, W. Liu, L. Zhang, X. Cao and X. Lu, An ultra-dense NiS_2/reduced graphene oxide composite cathode for high-volumetric/gravimetric energy density nickel–zinc batteries, *J. Mater. Chem. A*, 2019, **7**, 15654–15661.

7 L. Zhang, W. Liu, W. Shi, X. Xu, J. Mao, P. Li, C. Ye, R. Yin, S. Ye, X. Liu, X. Cao and C. Gao, Boosting lithium storage properties of MOF derivatives through a wet-spinning assembled fiber strategy, *Chem.–Eur. J.*, 2018, **24**(52), 13792–13799.

8 W. Hong, P. Ge, Y. Jiang, L. Yang, Y. Tian, G. Zou, X. Cao, H. Hou and X. Ji, Yolk-shell structured bismuth@N-doped carbon anode for lithium-ion battery with high volumetric capacity, *ACS Appl. Mater. Interfaces*, 2019, **11**(11), 10829–10840.

9 W. Liu, R. Yin, X. Xu, L. Zhang, W. Shi and X. Cao, Structural engineering of low-dimensional metal–organic frameworks: synthesis, properties, and applications, *Adv. Sci.*, 2019, 1802373.

10 Y. Jin, B. Zhu, Z. Lu, N. Liu and J. Zhu, Challenges and recent progress in the development of Si anodes for lithium-ion battery, *Adv. Energy Mater.*, 2017, **7**, 1700715.

11 Q. Xu, J. Y. Li, Y. X. Yin, Y. M. Kong, Y. G. Guo and L. J. Wang, Nano/micro-structured Si/C anodes with high initial coulombic efficiency in Li-ion batteries, *Chem.–Asian J.*, 2016, **11**, 1205–1209.

12 D. A. Agyeman, K. Song, G. H. Lee, M. Park and Y. M. Kang, Carbon-coated Si nanoparticles anchored between reduced graphene oxides as an extremely reversible anode material for high energy-density Li-ion battery, *Adv. Energy Mater.*, 2016, **6**, 1600904.

13 S. H. Cho, J. W. Jung, C. Kim and I. D. Kim, Rational design of 1-D Co_3O_4 nanofibers@low content graphene composite anode for high performance Li-ion batteries, *Sci. Rep.*, 2017, **7**, 45105.

14 H. Zhou, L. Zhang, D. Zhang, S. Chen, P. R. Coxon, X. He, M. Coto, H. K. Kim, K. Xi and S. Ding, A universal synthetic route to carbon nanotube/transition metal oxide nano-composites for lithium ion batteries and electrochemical capacitors, *Sci. Rep.*, 2016, **6**, 37752.

15 Y. Li, X. Hou, Y. Li, Q. Ru, S. Hu and K. Lam, The design and synthesis of polyhedral Ti-doped Co_3O_4 with enhanced lithium-storage properties for Li-ion batteries, *J. Mater. Sci.: Mater. Electron.*, 2016, **27**, 11439–11446.

16 L. Liu, L. Mou, J. Yu and S. Chen, Urchin-like CoO–C micro/nano hierarchical structures as high performance anode materials for Li-ion batteries, *RSC Adv.*, 2017, **7**, 2637–2643.

17 J. Guo, Y. Yang, W. Yu, X. Dong, J. Wang, G. Liu and T. Wang, Synthesis of α-Fe_2O_3, Fe_3O_4 and Fe_2N magnetic hollow nanofibers as anode materials for Li-ion batteries, *RSC Adv.*, 2016, **6**, 111447–111456.

18 J. H. Kim, Y. J. Hong, Y. C. Kang, Y. J. Choi and Y. S. Kim, Superior electrochemical properties of α-Fe_2O_3 nanofibers with a porous core/dense shell structure formed from iron acetylacetonate–polyvinylpyrrolidone composite fibers, *Electrochim. Acta*, 2015, **154**, 211–218.

19 U. Boesenberg, M. A. Marcus, A. K. Shukla, T. Yi, E. McDermott, P. F. Teh, M. Srinivasan, A. Moewes and J. Cabana, Asymmetric pathways in the electrochemical conversion reaction of NiO as battery electrode with high storage capacity, *Sci. Rep.*, 2014, **4**, 7133.

20 H. Lai, Q. Wu, J. Zhao, L. Shang, H. Li, R. Che, Z. Lyu, J. Xiong, L. Yang, X. Wang and Z. Hu, Mesostructured NiO/Ni composites for high-performance electrochemical energy storage, *Energy Environ. Sci.*, 2016, **9**, 2053–2060.

21 S. H. Park and W. J. Lee, Hierarchically mesoporous carbon nanofiber/Mn_3O_4 coaxial nanocables as anodes in lithium ion batteries, *J. Power Sources*, 2015, **281**, 301–309.

22 H. Liu, Z. H. Li, Y. R. Liang, R. W. Fu and D. C. Wu, Facile synthesis of MnO multi-core@ nitrogen-doped carbon shell nanoparticles for high performance lithium-ion battery anodes, *Carbon*, 2015, **84**, 419–425.

23 J. Z. Zhao, Z. L. Tao, J. Liang and J. Chen, Facile synthesis of nanoporous γ-MnO$_2$ structures and their application in rechargeable Li-ion batteries, *Cryst. Growth Des.*, 2008, **8**, 2799–2805.

24 C. Yan, G. Chen, X. Zhou, J. Sun and C. Lv, Template-based engineering of carbon-doped Co$_3$O$_4$ hollow nanofibers as anode materials for lithium-ion batteries, *Adv. Funct. Mater.*, 2016, **26**, 1428–1436.

25 S. Abouali, M. Akbari Garakani, B. Zhang, H. Luo, Z. L. Xu, J. Q. Huang, J. Huang and J. K. Kim, Co$_3$O$_4$/porous electrospun carbon nanofibers as anodes for high performance Li-ion batteries, *J. Mater. Chem. A*, 2014, **2**, 16939–16944.

26 X. Rui, H. Tan, D. Sim, W. Liu, C. Xu, H. H. Hng, R. Yazami, T. M. Lim and Q. Yan, Template-free synthesis of urchin-like Co$_3$O$_4$ hollow spheres with good lithium storage properties, *J. Power Sources*, 2013, **222**, 97–102.

27 L. Li, A. R. O. Raji and J. M. Tour, Graphene-wrapped MnO$_2$-graphene nanoribbons as anode materials for high-performance lithium ion batteries, *Adv. Mater.*, 2013, **25**, 6298–6302.

28 Y. Wu, X. Li, Q. Xiao, G. Lie, Z. Lie and J. Guan, The coaxial MnO$_2$/CNTs nanocomposite freestanding membrane on SSM substrate as anode materials in high performance lithium ion batteries, *J. Electroanal. Chem.*, 2019, **834**, 161–166.

29 Z. Cao, X. Chen, L. Xing, Y. Liao, M. Xu, X. Li, X. Liu and W. Li, Nano-MnO$_2$@TiO$_2$ microspheres: a novel structure and excellent performance as anode of lithium-ion batteries, *J. Power Sources*, 2018, **379**, 174–181.

30 R. Saravanan, S. Agarwal, V. K. M. M. Khan, F. Gracia, E. Mosquera, V. Narayanan and A. Stephen, Line defect Ce^{3+} induced Ag/CeO$_2$/ZnO nanostructure for visible-light photocatalytic activity, *J. Photochem. Photobiol., A*, 2018, **353**, 499–506.

31 D. Xiao, C. Lu, C. Chen and S. Yuan, CeO$_2$-webbed carbon nanotubes as a highly efficient sulfur host for lithium–sulfur batteries, *Energy Storage Mater.*, 2018, **10**, 216–222.

32 Q. Hao, G. Cui, Y. Tian, T. Tan and Y. Zhang, Three-dimensional S/CeO$_2$/rGO composites as cathode materials for lithium–sulfur batteries, *Materials*, 2018, **11**, 1720.

33 M. Li, X. Fan, X. Xiao, X. Huang, Y. Jiang and L. Chen, Ternary perovskite nickel titanate/reduced graphene oxide nano-composite with improved lithium storage properties, *RSC Adv.*, 2016, **6**, 61312–61318.

34 C. Yuan, H. Wang, J. Liu, Q. Wu, Q. Duan and Y. Li, Facile synthesis of Co$_3$O$_4$-CeO$_2$ composite oxide nanotubes and their multifunctional applications for lithium ion batteries and CO oxidation, *J. Colloid Interface Sci.*, 2017, **494**, 274–281.

35 S. Phokha, S. Hunpratub, N. Chanlek, S. Sonsupap and S. Maensiri, Synthesis, characterization and electrochemical performance of carbo/Ni-doped CeO$_2$ composites, *J. Alloys Compd.*, 2018, **750**, 788–797.

36 B. G. S. Raj, A. M. Asiri, J. J. Wu and S. Anandan, Synthesis of Mn$_3$O$_4$ nanoparticles via chemical precipitation approach for supercapacitor application, *J. Alloys Compd.*, 2015, **636**, 234–240.

37 S. Zhang, Y. Zhao, M. D. Somoano, J. Yang and J. Zhang, Synergistic mercury removal over the CeMnO$_3$ perovskite structure oxide as an SCR catalyst from coal combustion flue gas, *Energy Fuels*, 2018, **32**(11), 11785–11795.

38 H. Yi, J. Xu, X. Tang, S. Zhao, Y. Zhang, Z. Yang, J. Wu, X. Meng, J. Meng, H. Yan and Q. Li, Novel synthesis of Pd-CeMnO$_3$ perovskite based on unique ultrasonic intervention from combination of Sol–Gel and impregnation method for low temperature efficient oxidation of benzene vapour, *Ultrason. Sonochem.*, 2018, **48**, 418–423.

39 H. Li, G. Lu, Q. Dai, Y. Wang, Y. Guo and Y. Guo, Efficient low-temperature catalytic combustion of trichloroethylene over flower-like mesoporous Mn-doped CeO$_2$ microspheres, *Appl. Catal., B*, 2011, **102**, 475–483.

40 J. Bhagwan, A. Sahoo, K. L. Yadav and Y. Sharm, Nanofibers of spinel-CdMn$_2$O$_4$: a new and high performance material for supercapacitor and Li-ion batteries, *J. Alloys Compd.*, 2017, **703**, 86–95.

41 C. Li, R. Chen, X. Zhang, S. Shu, J. Xiong, Y. Zheng and W. Dong, Electrospinning of CeO$_2$–ZnO composite nanofibers and their photocatalytic property, *Mater. Lett.*, 2011, **65**, 1327–1330.

42 Y. Zhang, J. Li, Q. Li, L. Zhu, X. Liu, X. Zhong, J. Meng and X. Cao, Preparation of CeO$_2$–ZrO$_2$ ceramic fibers by electrospinning, *J. Colloid Interface Sci.*, 2007, **307**, 567–571.

43 X. Hu, Y. Ji, M. Wang, F. Miao, H. Ma, H. Shen and N. Jia, Water-Soluble and Biocompatible MnO@PVP Nanoparticles for MR Imaging In Vitro and In Vivo, *J. Biomed. Nanotechnol.*, 2013, **9**, 976–984.

44 Q. Cui, X. Dong, J. Wang and M. Li, Direct fabrication of cerium oxide hollow nanofibers by electrospinning, *J. Rare Earths*, 2008, **26**, 664–669.

45 Z. A. Elsiddig, D. Wang, H. Xu, W. Zhang, T. Zhang, P. Zhang, W. Tian, Z. Sun and J. Chen, Three-dimensional nitrogen-doped graphene wrapped LaMnO$_3$ nanocomposites as high-performance supercapacitor electrodes, *J. Alloys Compd.*, 2018, **740**, 148–155.

46 A. Younis, D. W. Chu and S. A. Li, Oxygen level: the dominant of resistive switching characteristics in cerium oxide thin films, *J. Phys. D: Appl. Phys.*, 2012, **45**, 355101.

47 L. R. Shah, B. Ali, H. Zhu, W. G. Wang, Y. Q. Song, H. W. Zhang, S. I. Shah and J. Q. Xiao, Detailed study on the role of oxygen vacancies in structural, magnetic and transport behavior of magnetic insulator: Co–CeO$_2$, *J. Phys.: Condens. Matter*, 2009, **21**, 486004.

48 M. Kumar, J. H. Yun, V. Bhatt, B. Singh, J. Kim, J. S. Kim, B. S. Kim and C. Y. Lee, Role of Ce^{3+} valence state and surface oxygen vacancies on enhanced electrochemical performance of single step solvothermally synthesized CeO$_2$ nanoparticles, *Electrochim. Acta*, 2018, **284**, 709–720.

49 D. R. Mullins, S. H. Overbury and D. R. Huntley, Electron spectroscopy of single crystal and polycrystalline cerium oxide surfaces, *Surf. Sci.*, 1998, **409**, 307–319.

50 A. Krittayavathananon, T. Pettong, P. Kidkhunthod and M. Sawangphruk, Insight into the charge storage mechanism and capacity retention fading of $MnCo_2O_4$ used as supercapacitor electrodes, *Electrochim. Acta*, 2017, **258**, 1008–1015.

51 G. Praline, B. E. Koel, R. L Hance, H. Lee and J. M. White, X-ray photoelectron study of the reaction of oxygen with cerium, *J. Electron Spectrosc. Relat. Phenom.*, 1980, **21**, 17–30.

52 C. Wang, D. L. Wang, Q. M. Wang and H. J. Chen, Fabrication and lithium storage performance of three-dimensional porous NiO as anode for lithium-ion battery, *J. Power Sources*, 2010, **195**, 7432–7437.

53 J. Wang, D. Jin, R. Zhou, X. Li, X. Liu, C. Shen, K. Xie, B. Li, F. Kang and B. Wei, Highly flexible graphene/Mn_3O_4 nanocomposite membrane as advanced anodes for Li-ion batteries, *ACS Nano*, 2016, **10**, 6227–6234.

54 X. Gu, J. Yue, L. Li, H. Xue, J. Yang and X. Zhao, General synthesis of MnO_x (MnO_2, Mn_2O_3, Mn_3O_4, MnO) hierarchical microspheres as lithium-ion battery anodes, *Electrochim. Acta*, 2015, **184**, 250–256.

55 X. Xu, R. Cao, S. Jeong and J. Cho, Spindle-like mesoporous α-Fe_2O_3 anode material prepared from MOF template for high-rate lithium batteries, *Nano Lett.*, 2012, **12**, 4988–4991.

56 C. Peng, B. Chen, Y. Qin, S. Yang, C. Li, Y. Zuo, S. Liu and Y. Yang, Facile ultrasonic synthesis of CoO quantum dot/graphene nanosheet composites with high lithium storage capacity, *ACS Nano*, 2012, **6**, 1074–1081.

57 H. Liu and Q. Le, Synthesis and performance of cerium oxide as anode materials for lithium ion batteries by a chemical precipitation method, *J. Alloys Compd.*, 2016, **669**, 1–7.

58 Y. Cho, P. Oh and J. Cho, A new type of protective surface layer for high-capacity Ni-based cathode materials: nanoscaled surface pillaring layer, *Nano Lett.*, 2013, **13**, 1145–1152.

59 K. B. Hatzell, M. Beidaghi, J. W. Campos, C. R. Dennison, E. C. Kumbur and Y. Gogotsi, A high performance pseudocapacitive suspension electrode for the electrochemical flow capacitor, *Electrochim. Acta*, 2013, **111**, 888–897.

60 C. Hua, X. Fang, Z. Wang and L. Chen, Lithium storage in perovskite lithium lanthanum titanate, *Electrochem. Commun.*, 2013, **32**, 5–8.

61 Y. Wang, X. Wen, J. Chen and S. Wang, Foamed mesoporous carbon/silicon composite nanofiber anode for lithium ion batteries, *J. Power Sources*, 2015, **281**, 285–292.